

Ultimate behavior of reinforced concrete cooling tower: Evaluation and comparison of design guidelines

Hyuk-Chun Noh[†]

*Department of Civil Engineering and Engineering Mechanics, Columbia University,
New York 10027, USA*

Chang-Koon Choi[‡]

Department of Civil and Environmental Engineering, KAIST, Daejeon 305-701, Korea

(Received July 21, 2005, Accepted November 29, 2005)

Abstract. Taking into account the geometrical and material nonlinearities, an ultimate behavior of reinforced concrete cooling tower shell in hyperbolic configuration is presented. The design wind pressures suggested in the guidelines of the US (ACI) and Germany (VGB), with or without the effect of internal suction, are employed in the analysis to examine the qualitative and quantitative characteristics of each design wind pressure. The geometrical nonlinearity is incorporated by the Green-Lagrange strain tensor. The nonlinear features of concrete, such as the nonlinear stress-strain relation in compression, the tensile cracking with the smeared crack model, an effect of tension stiffening, are taken into account. The biaxial stress state in concrete is represented by an improved work-hardening plasticity model. From the perspective of quality of wind pressures, the two guidelines are determined as highly correlated each other. Through the extensive analysis on the Niederaussem cooling tower in Germany, not only the ultimate load is determined but also the mechanism of failure, distribution of cracks, damage processes, stress redistributions, and mean crack width are examined.

Key words: reinforced concrete cooling tower; nonlinearity; ultimate load; design guidelines; damage index.

1. Introduction

Due to excellent performances and aesthetic beauty as well, the reinforced concrete (RC) shell structures have been used in various civil and architectural constructions. In regarding to the facilities in a nuclear power plant, the containment shell and cooling tower shell are the representative RC shell structures. The cooling tower shell is characterized by not only the thinness in shell thickness but also the hugeness in its dimension. In fact, the cooling tower shell definitely belongs to the largest and thinnest RC structures ever built on earth. One example of the largest cooling tower ever constructed is the Niederaussem tower in Germany that has 200 m in height and

[†] Research Associate, Corresponding author, E-mail: hcn2101@columbia.edu

[‡] Institute Chair Professor, E-mail: cck@kaist.ac.kr

130 m in diameter at the ground level (Busch *et al.* 2002, Noh *et al.* 2003).

As a structure having various features such as the thinness, intrinsic shape imperfection, pre-cracks, and an interference effect between cooling towers in group (Mahmoud 1993, Milford 1984), it had experienced two catastrophic collapse events in the past due to severe gusty wind: Ferrybridge towers in 1965 in United Kingdom and Ardeer tower in Scotland in 1973 (Milford 1984). The research on the structural behavior of a cooling tower shell is triggered by these two collapse events. And, numerous wind tunnel experiments and theoretical development have been performed to determine the wind pressure and corresponding behavior of this structure. In case of dynamic analysis on this structure, several research works (Choi 1999, Zahlten 1998) can be referred to. In this case, cyclic behavior (Kwak 2004, Cotsovos 2005) of concrete has to be included in the analysis to represent loading and unloading process.

In designing the RC cooling towers, two design guidelines, i.e., of the US (ACI 1985) and of Germany (VGB 1997), has been employed. Even though the overall distributions of the wind pressure distribution on the surface of a cooling tower shell are similar to each other, it is apparent that the two design guidelines give different wind pressure coefficients and corresponding wind pressure distributions. Accordingly, it will be informative to compare these two design guidelines in a qualitative and quantitative way as well by applying the wind pressures evaluated based on the respective guideline on the same cooling tower shell. In this study, the Niederaussem cooling tower shell is chosen as an example structure.

In the analysis, various nonlinearities, such as the material nonlinearity of concrete and reinforcing steel, the geometrical nonlinearities due to a large displacement, a tensile cracking, and an effect of tension stiffening are taken into account. The biaxial behavior of concrete is represented by a work-hardening plasticity model that is improved to reproduce the ductility increase effect in the biaxial stress state. The cracking in concrete is assumed to be smeared into the domain of a finite element. The steel reinforcement is assumed to behave in one dimension and is modeled as bilinear material. As a nonlinear control scheme, the arc-length control (Crisfield 1983) is applied with which the energy releasing phenomenon during loading process can be checked. For the numerical modeling of the reinforced concrete shell structure, a degenerated layered shell element (Choi 1994, 1996a) is employed. The effects of thermal or hygric loading that correspond to the initial cracking in the shell are not taken into consideration. Even though there can be some geometrical specialties, such as flue-gas inflow (Busch *et al.* 2002), and some special features including non-homogeneous soil-situation and the high-performance acid-resistance concrete, a cooling tower shell in general shape and in general environmental condition has been taken into consideration.

2. Numerical models for materials

2.1 Occurrence of cracks

Adopting a smeared crack model, the cracks are assumed to be formed in a distributed pattern in the continuum level when the principal stress exceeds the tensile capacity f_t' of the concrete. Once the cracks are formed, the elasticity modulus and the Poisson's ratio are set as zero in the crack normal direction and the cracked shear moduli are applied.

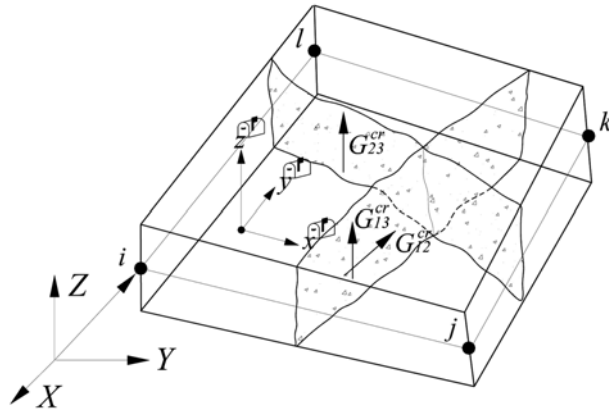


Fig. 1 Shear modulus in cracked section

2.2 Shear transfer

According to experimental investigations, crack width is the most important factor affecting shear transfer in cracked concrete. In this study, following formulae are adopted for the cracked shear moduli with a shear retention factor $\beta = 0.25$ (Hand *et al.* 1973):

$$G_{ij}^{cr} = F(G, \beta, \varepsilon_c, \varepsilon_u = 0.004) \quad (1)$$

As is seen in Eq. (1), the maximum strain in the crack normal direction, to maintain the shear transfer capability, is assumed as $\varepsilon_u = 0.004$. The constitutive matrices for concrete cracked in one and two directions, $\mathbf{D}_{cr}^{(1)}$, $\mathbf{D}_{cr}^{(2)}$, are assumed as follows:

$$\mathbf{D}_{cr}^{(1)} = \begin{bmatrix} 0 & & & & & \\ & E & & & & \\ & & G_{12}^{cr} & & & \\ & & & G_{13}^{cr} & & \\ & & & & \frac{5}{6}G & \\ & & & & & G_{23}^{cr} \end{bmatrix}, \quad \mathbf{D}_{cr}^{(2)} = \begin{bmatrix} 0 & & & & & \\ & 0 & & & & \\ & & G_{12:\min}^{cr} & & & \\ & & & G_{13}^{cr} & & \\ & & & & \frac{5}{6}G & \\ & & & & & G_{23}^{cr} \end{bmatrix} \quad (2)$$

where $G_{12:\min}^{cr} = 0.5\text{Min}(G_{13}^{cr}, G_{23}^{cr})$. The cracked shear moduli are depicted in Fig. 1.

2.3 Constitutive relation for cracked concrete with crack rotation

It has been observed that the crack direction is not fixed but rotates complying with the stress state in concrete (Gupta 1984), affecting the stiffness of the concrete elements. Accordingly, the rotating crack model is employed. For concrete element cracked in one direction, the constitutive matrix is well defined with the aid of geometric matrix \mathbf{G}_{cr} (Gupta 1984) and the incremental relationship is given as follows:

$$\Delta\sigma_{\bar{x}} = \mathbf{D}_{c1}^{cr}\Delta\varepsilon_{\bar{x}} = [\bar{\mathbf{D}}_{c1} + \mathbf{G}_{cr}]\Delta\varepsilon_{\bar{x}} \quad (3)$$

where $\bar{\mathbf{D}}_{c1}$ is given by the coordinate transformation of Eq. (2) to local coordinate system \bar{x} (Fig. 1). While the matrix $\bar{\mathbf{D}}_{c1}$ consists of contributions from axial and shear resistances, the constitutive matrix for the concrete cracked in two directions, $\bar{\mathbf{D}}_{c2}$, is derived as having only the contribution from the shear resistance. The constitutive relation for this case reads (Noh 2005, 2006),

$$\mathbf{D}_{c2}^{cr} = [\bar{\mathbf{D}}_{c2} + \mathbf{G}_{cr}] \quad (4)$$

2.4 Tension stiffening

In order to take into account the effect of tension stiffening, the model with tension cut-off strategy is employed (Owen 1980). In this model, the ultimate strain ε_m , given as constant TS times the tensile strain ε_s , controls the degree of tension stiffening. In this study, TS = 20.0, which is chosen from example analyses that matches the experimental results well, is employed exclusively

2.5 Yielding of concrete in biaxial stress state

To represent the behavior of concrete in biaxial compression, a work-hardening plasticity model is adopted. In this model, the initial yield surface and the subsequent yield (or loading) surfaces as well is defined (Hinton 1984), i.e., the yield surface is not fixed and the stresses are allowed to go outside the yield surface. For the definition of yield, the Drucker-Prager yield criterion is adopted: $f(I_1, J_2) = \sqrt{\alpha I_1 + \beta(3J_2)} = \sigma_o$, where σ_o signifies effective stress. This model, however, does not reproduce the ductility increase effect of concrete under biaxial stress state. In order to overcome this shortcoming and consequently to improve the performance of the plasticity model, a relationship between stress ratio and strain multiplier is established as $\varphi = 5.2r_s + 2.0$ where $r_s = \sigma_2/\sigma_1$. The strain multiplier φ signifies a number multiplied to the elastic compressive strain $\varepsilon_e = f'_c/E_o$. Applying the normality condition in an associated flow rule, the elasto-plastic stress-strain relationship D_{ijkl}^{ep} is determined to be

$$d\sigma_{ij} = D_{ijkl}^{ep}d\varepsilon_{kl} = \left(D_{ijkl}^e - \frac{D_{ijst}^e \left(\frac{\partial f}{\partial \sigma_{uv}} \right) \left(\frac{\partial f}{\partial \sigma_{st}} \right) D_{uvkl}^e}{H + \left(\frac{\partial f}{\partial \sigma_{mn}} \right) D_{mnop}^e \left(\frac{\partial f}{\partial \sigma_{op}} \right)} \right) d\varepsilon_{kl} \quad (5)$$

where f and H denote an yield function and a hardening parameter, respectively. Since the crushing of concrete is a phenomenon governed by strain, it is presumed to be traced by the strain dual of the yield function where σ_o is substituted by ε_m , the ultimate strain.

2.6 Steel reinforcement

Despite the fact that reinforcements in the layered concrete shell element are modeled as plane layers, the actual in-situ embedding of the reinforcement is one dimensional. Therefore it is not necessary to introduce complex multidimensional constitutive relationships for the reinforcement, and therefore a model of one-dimensional bilinear approximation is chosen.

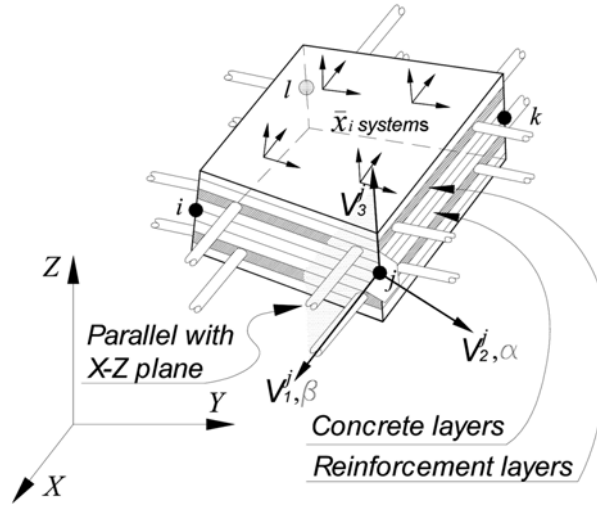


Fig. 2 4-node degenerated layered shell element

2.7 Degenerated shell finite element

For the numerical modeling of a cooling tower, a 4-node degenerated layered shell element (Choi 1994, 1996a) is adopted. This shell element employs an assumed shear strain field to eliminate locking problems that arise as the shell thickness is reduced, and shows improved behavior without locking phenomena in membrane and shear. The layering scheme and various coordinate systems that are required to define the stress and strain are shown in Fig. 2.

In order to define the displacement vector \mathbf{u} , in addition to the three translational degrees of freedom u, v, w at the mid-surface, two rotational degrees of freedom α and β along the nodal vectors $\mathbf{V}_2^i, \mathbf{V}_1^i$, which are normal to the nodal vector \mathbf{V}_3^i , have to be used as follows:

$$\mathbf{u} = \begin{Bmatrix} u \\ v \\ w \end{Bmatrix} = \sum_{i=1}^4 N_i(\xi, \eta) \begin{Bmatrix} u_i \\ v_i \\ w_i \end{Bmatrix}_{mid} + \sum_{i=1}^4 N_i(\xi, \eta) \frac{\zeta h_i}{2} \begin{bmatrix} V_{1x}^i & -V_{2x}^i \\ V_{1y}^i & -V_{2y}^i \\ V_{1z}^i & -V_{2z}^i \end{bmatrix} \begin{Bmatrix} \alpha_i \\ \beta_i \end{Bmatrix} \quad (6)$$

The mathematical definitions of nodal vectors $\mathbf{V}_2^i, \mathbf{V}_1^i$ and \mathbf{V}_3^i can be found in Choi (1994) and are illustrated in Fig. 2.

Applying the stationary condition on the total potential energy consisting of contributions from membrane, bending, shear and external loads, the element stiffness can be formed as follows:

$$\mathbf{K}_c = \int_V \mathbf{B}_c^T \mathbf{D}_c \mathbf{B}_c dV; \quad c = \begin{cases} m: \text{membrane} \\ b: \text{bending} \\ s: \text{shear} \end{cases} \quad (7)$$

In this study, an implicit layering scheme, introduced by Lin and Scordelis (1975), is adopted to

model the reinforced concrete shell structures. In this scheme, the evaluation of the element stiffness consists of through-thickness integrations of each layer and area integrations. The number of layers is reported to be sufficient from 6 to 10 for each element (Min 1992, Hinton 1984). Accordingly, 10 concrete layers plus the 4 steel layers, 2 inner and outer layers respectively, are used exclusively.

3. Geometrical nonlinearity

3.1 Stress-strain matrix

The geometrical nonlinearity comes from the Green-Lagrange strain tensor that can be divided into linear infinitesimal and nonlinear large displacement components as follows:

$$\boldsymbol{\varepsilon} = \boldsymbol{\varepsilon}^L + \boldsymbol{\varepsilon}^{NL} = \left(\mathbf{H} + \frac{1}{2}\mathbf{A} \right) \bar{\boldsymbol{\delta}} \quad (8)$$

where the vector $\bar{\boldsymbol{\delta}}$ is given as $\bar{\boldsymbol{\delta}} = \langle \mathbf{E}_{\bar{x}} \ \mathbf{E}_{\bar{y}} \ \mathbf{E}_{\bar{z}} \rangle^T$ with $\mathbf{E}_{\bar{i}} = \langle \bar{u}_{,\bar{i}} \ \bar{v}_{,\bar{i}} \ \bar{w}_{,\bar{i}} \rangle^T$, $\bar{i} = \bar{x}, \bar{y}, \bar{z}$. Matrices \mathbf{H} and \mathbf{A} can be found in (Choi 1996a, Noh 2005). Taking the variation of Eq. (8), we can get

$$d\boldsymbol{\varepsilon} = d(\mathbf{H}\bar{\boldsymbol{\delta}}) + \frac{1}{2}d(\mathbf{A}\bar{\boldsymbol{\delta}}) = (\mathbf{H} + \mathbf{A})\mathbf{G}d\mathbf{a} \quad (9)$$

where $\bar{\boldsymbol{\delta}} = \mathbf{G}\mathbf{a}$, and \mathbf{G} contains the shape functions as coefficients and the vector \mathbf{a} consists of all nodal variables. Consequently, the strain-displacement matrix can be obtained as follows:

$$\bar{\mathbf{B}} = \mathbf{B}_L + \mathbf{B}_{NL} = (\mathbf{H} + \mathbf{A})\mathbf{G} \quad (10)$$

3.2 Expression for tangential stiffness

Taking variation of the residual force $\mathbf{R} = \mathbf{F} - \int_V \bar{\mathbf{B}}^T \boldsymbol{\sigma} dV$, the tangential stiffness can be derived as follows:

$$\begin{aligned} \mathbf{K}_T d\mathbf{a} &= \int_V d\mathbf{B}_{NL}^T \boldsymbol{\sigma} dV + \int_V \mathbf{B}_L^T \mathbf{D} \bar{\mathbf{B}} dV d\mathbf{a} + \int_V \mathbf{B}_{NL}^T \mathbf{D} \bar{\mathbf{B}} dV d\mathbf{a} \\ &= \mathbf{K}_\sigma d\mathbf{a} + \bar{\mathbf{K}} d\mathbf{a} \end{aligned} \quad (11)$$

where $d\mathbf{F} = \mathbf{K}_T d\mathbf{a}$ and $\int_V d\mathbf{B}_{NL}^T \boldsymbol{\sigma} dV = \mathbf{K}_\sigma d\mathbf{a}$ are used. Accordingly, the tangential stiffness is found to be $\mathbf{K}_T = \mathbf{K}_\sigma + \bar{\mathbf{K}}$. Furthermore, the matrix $\bar{\mathbf{K}}$ can be rearranged as $\bar{\mathbf{K}} = \mathbf{K}_L + \mathbf{K}_{LD}$ if the relation of $\bar{\mathbf{B}} = \mathbf{B}_L + \mathbf{B}_{NL}$ is considered. Therefore, one can note that the tangential stiffness matrix \mathbf{K}_T consists of the linear contribution \mathbf{K}_L , stress dependent geometric stiffness \mathbf{K}_σ plus the term representing the effect of the large displacement \mathbf{K}_{LD} .

3.2.1 Geometric stiffness

The geometric stiffness matrix accounts for the effects of membrane forces and is influenced only by the element geometry, the displacement field and the state of stress. With the variation of the strain-displacement matrix \mathbf{B}_{NL} in Eq. (10), the geometric stiffness is derived as

$$\mathbf{K}_\sigma d\mathbf{a} = \int_V \mathbf{G}^T \mathbf{S} \mathbf{G} dV d\mathbf{a} \quad (12)$$

The matrix \mathbf{S} is defined by the Kronecker product of Σ and \mathbf{I} as follows:

$$\mathbf{S}_{9 \times 9} = \Sigma_{3 \times 3} \otimes \mathbf{I}_{3 \times 3}; \quad \Sigma_{3 \times 3} = \begin{bmatrix} \sigma_x & \tau_{xy} & \tau_{xz} \\ & \sigma_y & \tau_{yz} \\ \text{symm.} & & 0 \end{bmatrix}, \quad \mathbf{I}_{3 \times 3} = \begin{bmatrix} 1 & & \\ & 1 & \\ & & 1 \end{bmatrix} \quad (13)$$

4. Comparison of wind pressures

4.1 Design wind pressure of VGB

In the German guideline for cooling tower construction, VGB (1997), the wind pressure is defined as

$$P(z, \Theta) = \varphi q(z) C_p(\Theta), \quad q(z) = 0.9(z/10)^{0.22} \quad (14)$$

where the dynamic amplification factor φ is 1.07. The exponent 0.22 in Eq. (14) corresponds to a terrain with low surface roughness. The pressure is calculated in the dimension of kN/m^2 . The minimum pressure coefficient C_p is determined depending on the ratio of the shell thickness 'k' to the meridional rib distance 'a', and divided into 5 categories in accordance with the roughness of the shell surface: K1.0, K1.1, K1.2, K1.3, and K1.4. The equations for circumferential distribution of wind pressure coefficients are given in Table 1. When the effect of internal suction is taken into account, the pressure coefficients in Table 1 are added by 0.5.

Table 1 Equations for pressure coefficient (VGB)

Curve	Min. C_p	Zone I	Zone II	Zone III
K1.0	-1.0	$1 - 2.0 \left(\sin \frac{90^\circ}{70^\circ} \Theta \right)^{2.267}$	$-10 + 0.5 \left(\sin \frac{90^\circ}{21^\circ} (\Theta - 70) \right)^{2.395}$	-0.5
K1.1	-1.1	$1 - 2.1 \left(\sin \frac{90^\circ}{71^\circ} \Theta \right)^{2.239}$	$-1.1 + 0.6 \left(\sin \frac{90^\circ}{22^\circ} (\Theta - 71) \right)^{2.395}$	-0.5
K1.2	-1.2	$1 - 2.2 \left(\sin \frac{90^\circ}{72^\circ} \Theta \right)^{2.205}$	$-1.2 + 0.7 \left(\sin \frac{90^\circ}{23^\circ} (\Theta - 72) \right)^{2.395}$	-0.5
K1.3	-1.3	$1 - 2.3 \left(\sin \frac{90^\circ}{73^\circ} \Theta \right)^{2.166}$	$-1.3 + 0.8 \left(\sin \frac{90^\circ}{24^\circ} (\Theta - 73) \right)^{2.395}$	-0.5
K1.4	-1.4	$1 - 2.4 \left(\sin \frac{90^\circ}{74^\circ} \Theta \right)^{2.213}$	$-1.4 + 0.9 \left(\sin \frac{90^\circ}{25^\circ} (\Theta - 74) \right)^{2.395}$	-0.5

Table 2 Fourier coefficients for pressure coefficient (ACI)

n	A_n	n	A_n
0	-0.11670, 0.38330(case of no internal suction)		
1	-0.27918	7	-0.04474
2	-0.61978	8	-0.00833
3	-0.50927	19	-0.00972
4	-0.09167	10	-0.01356
5	0.11794	11	-0.00597
6	0.03333	12	-0.01667

4.2 Design wind pressure of ACI

In the ACI code, the wind pressure is expressed as $p(\theta, z) = q_o G(\theta) M(z)$. The dynamic head is given as $q_o = (1/2)\rho_a v_{10}^2$. The air density is $\rho_a = 0.126 \text{ kg/m}^3$ and v_{10} = design wind velocity (40.2 m/sec²). The two functions $G(\theta)$ and $M(z)$, which express the circumferential and meridional distributions of wind pressure respectively, are as follows:

$$G(\theta) = \sum_{n=0}^{12} A_n \cos(n\theta), \quad M(z) = \left(\frac{z}{10}\right)^{\frac{2}{7}} \tag{15}$$

where z is in the dimension of meter. The circumferential distribution is given as a Fourier expression and the Fourier coefficients A_n 's are given in Table 2. In the ACI code, the effect of internal suction is taken into account by a modification only of A_0 , as given in Table 2.

4.3 Pressure distributions

In Figs. 3 and 4, the distributions of the wind pressure coefficients and wind pressure in the circumference at the throat level are illustrated. While the pressure coefficients are almost similar to

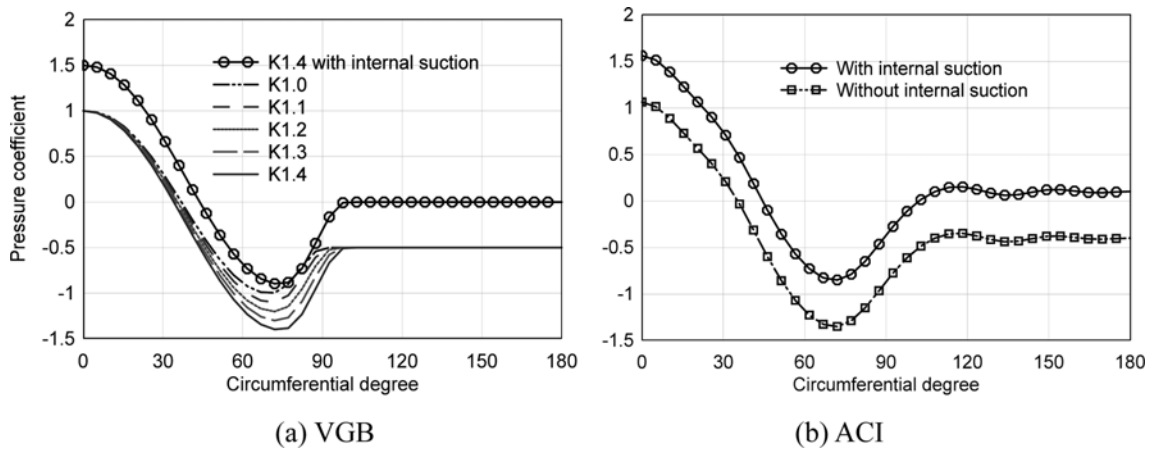


Fig. 3 Pressure coefficients distributions

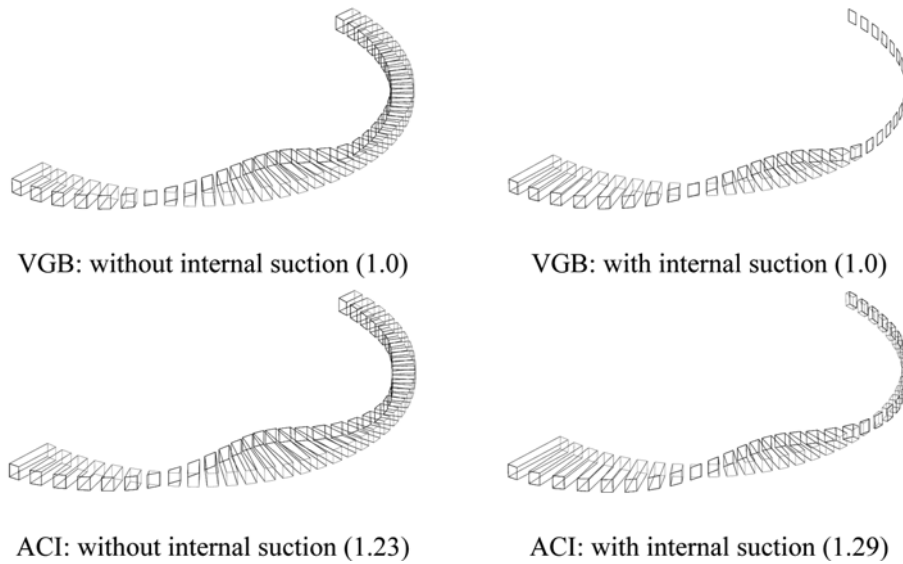


Fig. 4 Comparison of wind pressure distributions (at throat). Note: The maximum wind pressures are normalized to VGB and are given in the parentheses.

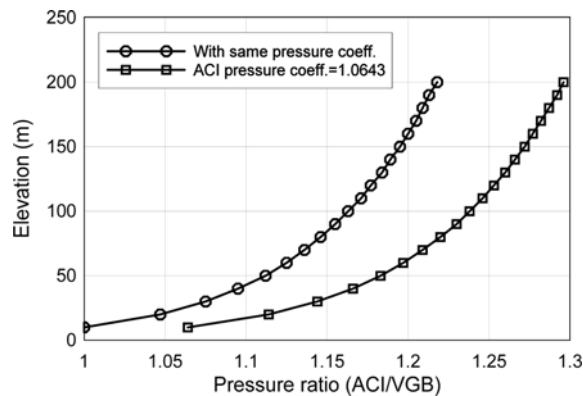


Fig. 5 Pressure ratio as a function of elevation

each other, the amount of wind pressure shows some discrepancies caused by the different exponents in $q(z)$ (VGB) and $M(z)$ (ACI).

Fig. 5 shows the ratio of pressure in ACI-code to the pressure in VGB-code as a function of elevation at the windward meridian. The line with circle is evaluated directly from the two equations $q(z)$ (VGB) and $M(z)$ (ACI), whilst the curve with rectangle is computed based on the actual pressure coefficients given in Table 2, which has 1.0643 at the stagnation. As is noted in Fig. 5, the pressure based on ACI is larger over 20% than that of VGB. In case of VGB, the curve K1.4 is adopted. Even though we have employed the same surface roughness conditions in each guideline, it has to be noticed that the wind pressure in the U.S. is bound to be greater than in Europe because of the hard meteorological condition, such as hurricanes, tornados, and so on.

Table 3 Parameters of meridional equation of Niederaussem cooling tower

	R_o	a	b
Upper shell	42.3703	0.2597	8.2940
Lower shell	-7.2434	49.8735	114.9326

5. Evaluation of ultimate load bearing capacity

5.1 Geometry and material properties

The ultimate behavior of Niederaussem cooling tower subjected to the design wind pressure is investigated. The interference effect due to a grouping is not considered and a soloist cooling tower is taken into account. The meridional equation of this cooling tower is given as follows:

$$R(z) = R_o + \frac{a}{b} \sqrt{b^2 + (H_t - z)^2} \quad (16)$$

The elevation of the throat, H_t , is 142.0 m and the other parameters are given in Table 3 for upper and lower parts of the tower shell. The diameters at the base, top and throat are 136.0 m, 88.41 m, and 85.26 m, respectively. The total surface area of the shell reaches over 60,000 m² (Busch *et al.* 2002).

The material constants for concrete and steel reinforcement are as follows: $E_c = 30.0$ GPa, $f'_c = 21.186$ MPa, $f_t = 2.4$ MPa, $\nu = 0.2$, $E_s = 210.0$ GPa, $f_y = 500.0$ MPa. The specific weight of reinforced concrete is assumed as $\gamma_c = 24.25$ kN/m³.

5.2 Nonlinear behavior of Niederaussem cooling tower shell

The Niederaussem cooling tower is modeled with 1365 (35 × 39) shell finite elements and 1480 (37 × 40) nodes. Considering symmetries in the structure and applied wind load, a half model is employed. The base columns are excluded from the finite element model and assumed as hinge supports as has been done in the literature (Choi 1996b, Hara *et al.* 1994, Mahmoud 1993, Milford 1984, Min 1992). In modeling the wind pressure, however, the column height is taken into account because the column height affects the wind intensity. Fig. 6 shows the full model of the cooling tower and the variation of shell thickness along the meridian. In the finite element mesh, the uppermost edge member of the tower is converted into a single array of shell finite elements having a certain thickness that has equivalent bending stiffness to the original shape. The detailed configuration of the top edge can be found in Busch *et al.* (2002).

Considering the fact that the self-weight is applied long before the exertion of the wind pressure, making the cooling tower is in the pre-stressed state, the following loading scheme has to be employed:

$$G_p + \lambda W_d \quad (17)$$

where the subscript p , d denote pre- and design load, and λ signifies a load factor, a multiplier to the design wind pressure. The gravity load G_p , which is caused by the self-weight of the cooling tower, acts as a counter resistance to the tensile action, induced by the wind pressure, ensuring *a priori* safety to cooling tower structures.

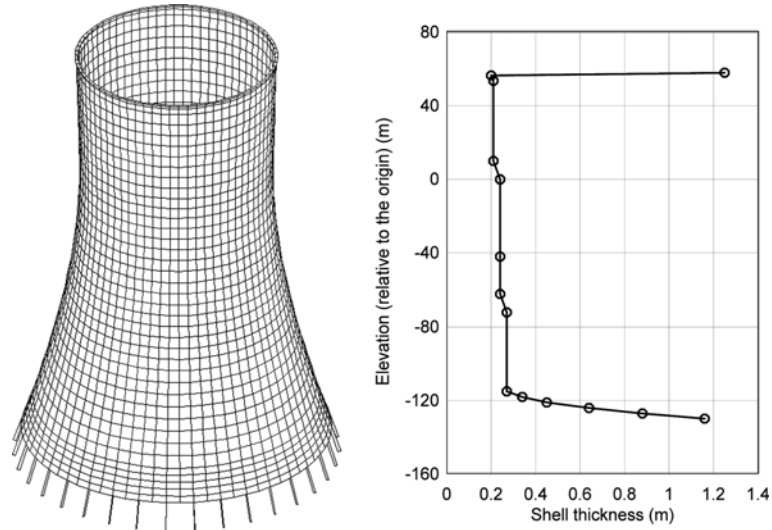


Fig. 6 Full model of Niederaussem cooling tower and its thickness variation. Note: The elevation is given referencing the throat as an origin.

5.2.1 Load-displacement history

The load-displacement relationships at the throat in the windward part are shown in Fig. 7 for four different loading cases: based on VGB-guidelines with and without the effect of internal suction, and ACI-code-based wind pressure with and without internal suction. The basic difference between VGB and ACI is shown by discrepancies in the ultimate load factor, which is expected in advance from section 4 and Fig. 5 where comparisons are made for wind pressures of respective guidelines. In both guidelines, the effect of internal suction is revealed to be relatively small. The ultimate load factor has reached up to 2.254(VGB) and 1.910(ACI) when the tension stiffening parameter $TS = 20.0$. The throat displacement is obtained to be about 80cm. In the works of Busch *et al.* (2002) and Noh *et al.* (2003), the ultimate load factor is obtained as 2.37 with throat displacement of about 1.9 m, where the VGB-guidelines are employed. The nonlinear behavior is

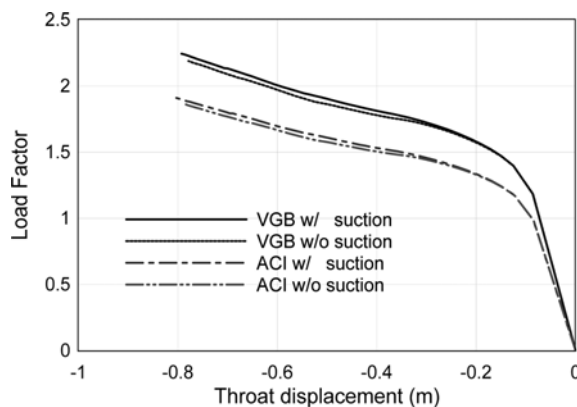


Fig. 7 Load-displacement path

observed to be initiated by the occurrence of cracks at the load levels of 1.185 (VGB) and 0.985(ACI).

5.2.2 Crack patterns

In Figs. 8(a) and (b), crack patterns in the outer-most layer are given at the failure load for VGB and ACI guidelines respectively. In case of the extrados, almost all the cracks are formed as thru-thickness horizontal ones, while some doubly cracked elements appear on the intrados where deformation happens in a concave shape. The crack patterns, however, does not give any useful information on the status of a structure without the evaluation of the crack width. The crack width tells us on what state the deterioration and serviceability of the RC structure is.

As the smeared crack model is employed in the analysis, the crack width can only be measured in the mean sense using the total principal strain ε_{pr} . Referring to Fig. 9, the crack strain can be given as

$$\varepsilon_{cr} = (\varepsilon_{pr} - \varepsilon_e) + \varepsilon_{bs} + \varepsilon_{er} \quad (18)$$

where ε_e stands for elastic strain and ε_{bs} , ε_{er} signify strains relative to a bond slip and elastic recovery, respectively. In this study, $\varepsilon_{bs} + \varepsilon_{er}$ is simply ignored due to the lack of experimental and theoretical data, which leads the mean crack width to be the possible minimum estimation.

The distributions of mean crack width that is evaluated based on Eq. (18) are shown in Fig. 10. In order to show clearly the relative quantities, the strains are magnified 10^4 times and designated as the height of a plane-normal hexahedron. The maximum crack width at the failure is observed as occurred in the element at the throat, where the thickness takes its minimum (21 cm) and the reinforcement ratio is also small. Accordingly, the yielding of meridional reinforcement occurs at

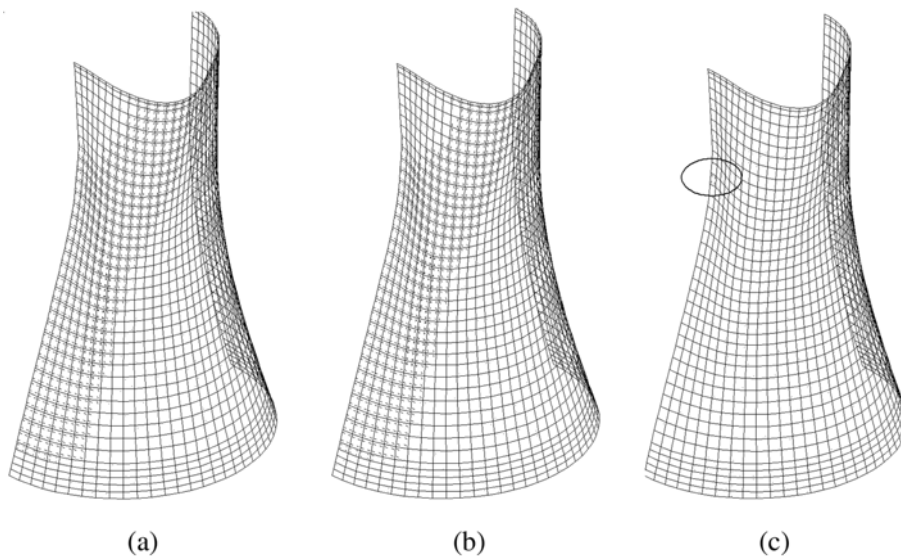


Fig. 8 Crack patterns and yielding of reinforcement at the failure load (deformation magnified 20 times): (a) VGB (2.254), (b) ACI (1.910), (c) yielding of reinforcement

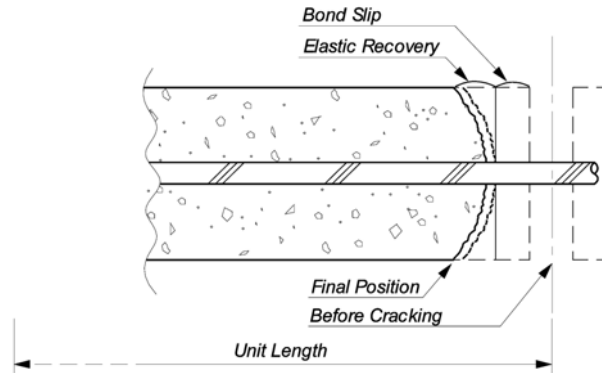


Fig. 9 Mean crack width approximation in the smeared crack model

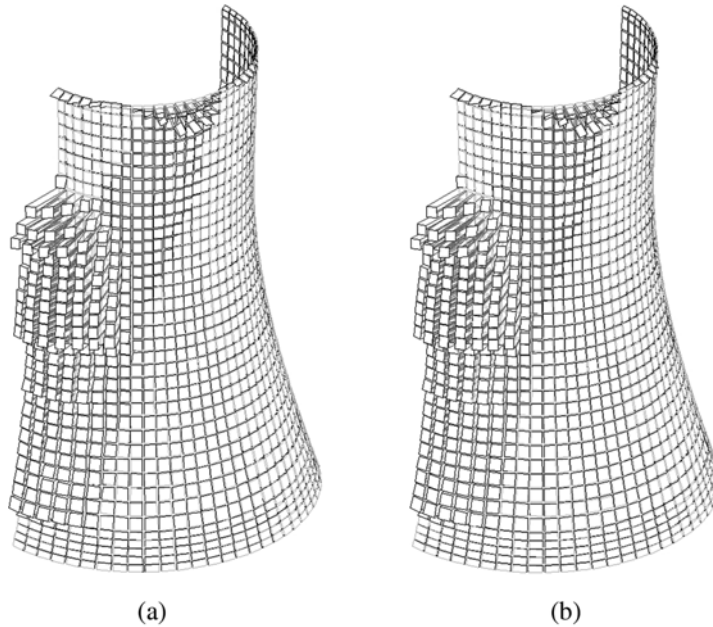


Fig. 10 Iso-plot of mean crack width (extrados)

this point resulting in the commencement of failure phase of the cooling tower. The width of bending crack on the extrados, in the diagonal direction, is examined to be relatively small when compared with those in the windward part, showing only about one-fiftieth in magnitude.

5.2.3 Damage index

If we define a stiffness index S_i at the i -th loading step as

$$S_i = \frac{\mathbf{P}_i^T \delta_i}{\delta_i^T \delta_i} \quad (19)$$

where \mathbf{P}_i and δ_i are incremental applied load and incremental displacement at the i -th step, a ratio of

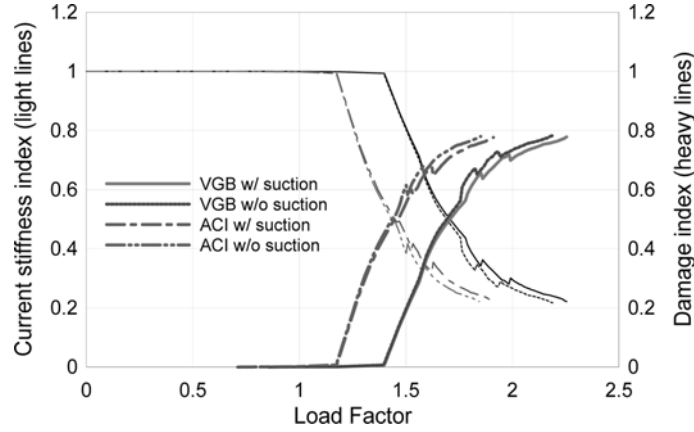


Fig. 11 Evolution of current stiffness and damage indexes

stiffness index of current (n -th) step to that of initial (elastic) step will give the current stiffness index C_n at the current step as follows:

$$C_n = \frac{\mathbf{P}_n^T \boldsymbol{\delta}_n}{\boldsymbol{\delta}_n^T \boldsymbol{\delta}_n} / \frac{\mathbf{P}_e^T \boldsymbol{\delta}_e}{\boldsymbol{\delta}_e^T \boldsymbol{\delta}_e} \quad (20)$$

where \mathbf{P}_e and $\boldsymbol{\delta}_e$ are applied load and displacement in the elastic range that corresponds to the initial step of the full nonlinear analysis. In other words, the current stiffness index C_n gives a relative value of stiffness of the damaged structure to that of the intact one as weighted by means of the displacement. As natural, the current stiffness index in the range of elastic behavior is the same as unity, indicating no damages.

In Fig. 11, the evolution of current stiffness index of the cooling tower under consideration is given as a function of a load factor for four different loading cases. The trend of variation is observed as similar with each other for VGB and ACI loadings. Even though there appear some gain and loss of stiffness along the loading history, the current stiffness at the failure reaches about 20% of the initial stiffness. In the perspective of that the current stiffness index gives the degradation of the global stiffness, it can be used to determine the degree of damage of a structure because the load bearing capacity of a structure is determined by its structural stiffness. The damage index D_n can, therefore, be defines as follows:

$$D_n = 1 - C_n \quad (21)$$

As noted by Harte *et al.* (2000), the progressive damage phenomena have to be based on the load- or time-evolution of the global stiffness matrix. In this sense, the damage index D_n offers a direct basis for determining the degree of damage because it is given as a function of the current stiffness index. In Fig. 11, the damage index is also given with heavy lines as a function of load factor λ .

5.2.4 Close investigation on failure procedure

The failure of the cooling tower is observed to be initiated by the yielding of the meridional reinforcement at the throat (The yielding pattern of reinforcement is shown in Fig. 8(c)), and then

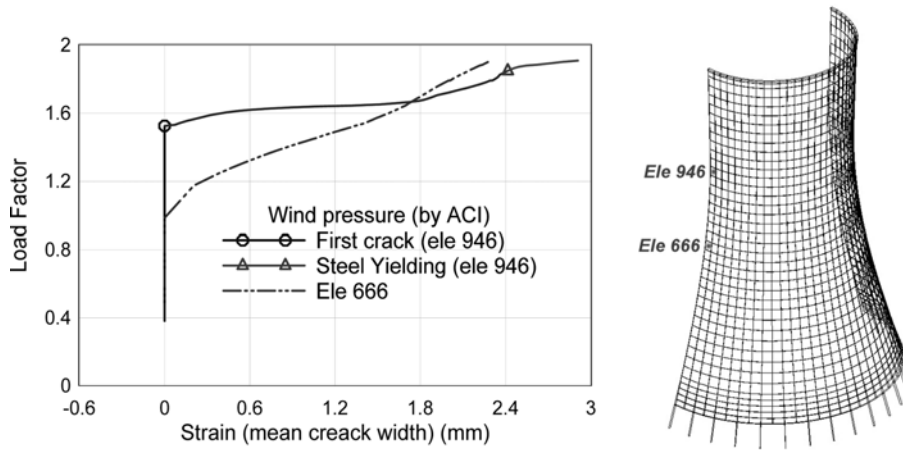


Fig. 12 Variation of mean crack width in the elements 666 (100 m) and 946 (142 m)

the crushing (in tension) around yielding zone dominates the failure. In Fig. 12, the total strains at the two specific locations are shown for ACI loading. In case of the element 946 (elevation = 142 m: throat level), the total strain reaches the yield level at the load factor 1.85 (at the mean crack width of 2.38 mm) and proceeds to 1.910 (with the mean crack width of about 2.9 mm). In case of the element 666 (elevation = 100 m), where the first crack is occurred, the total strain does not reach the yield level. It has to be noticed in Fig. 12 that the increase in strain in the element 946 is relatively fast and the strain reaches the level of yielding in a short range of load increment: from 1.53 to 1.85.

5.2.5 Stress redistribution

As the load-displacement histories between VGB and ACI loadings are similar to each other, so are the stress distributions. The only difference between the two is the load factor. Accordingly, only

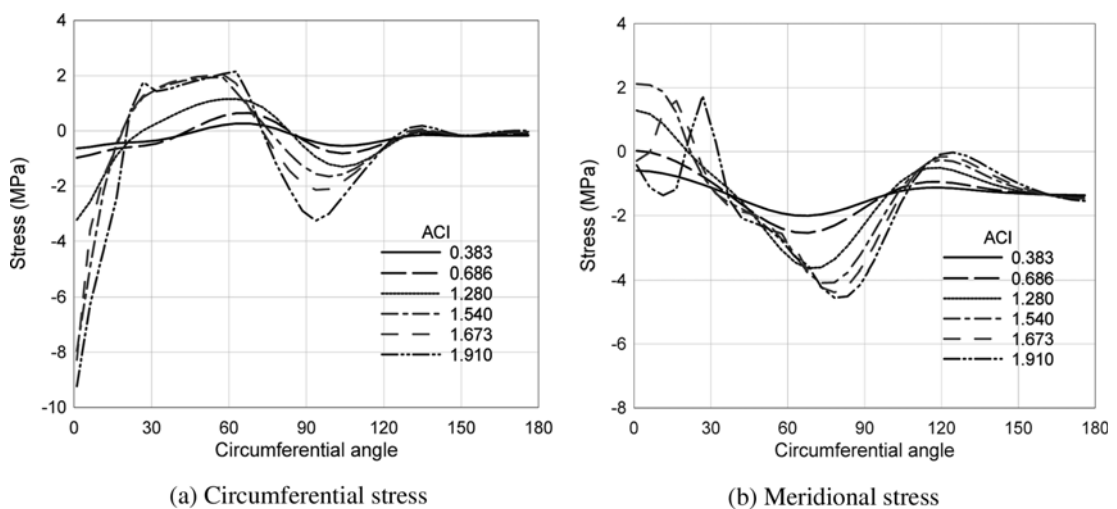


Fig. 13 Stresses in the array of elements along the circumference (throat level)

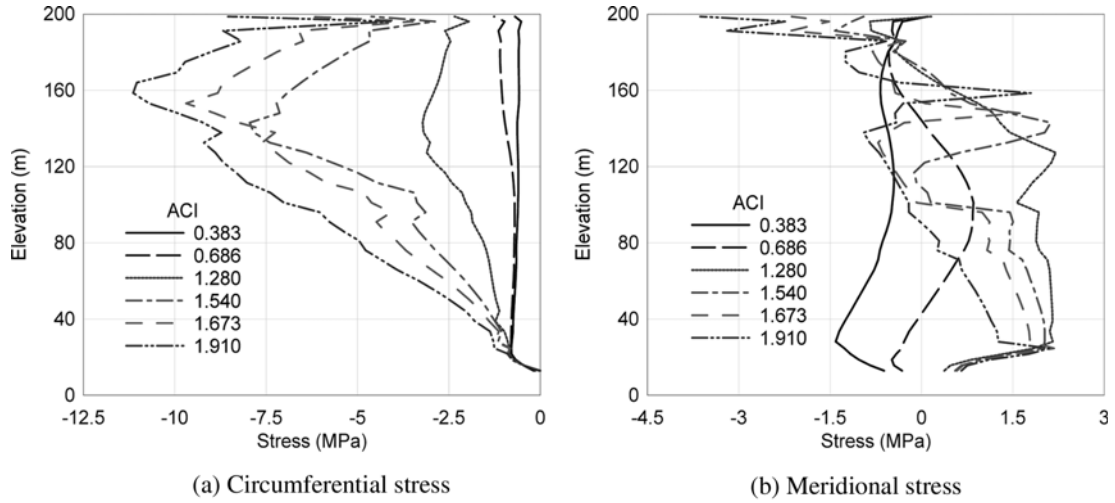


Fig. 14 Stresses in the array of elements along the meridian (windward)

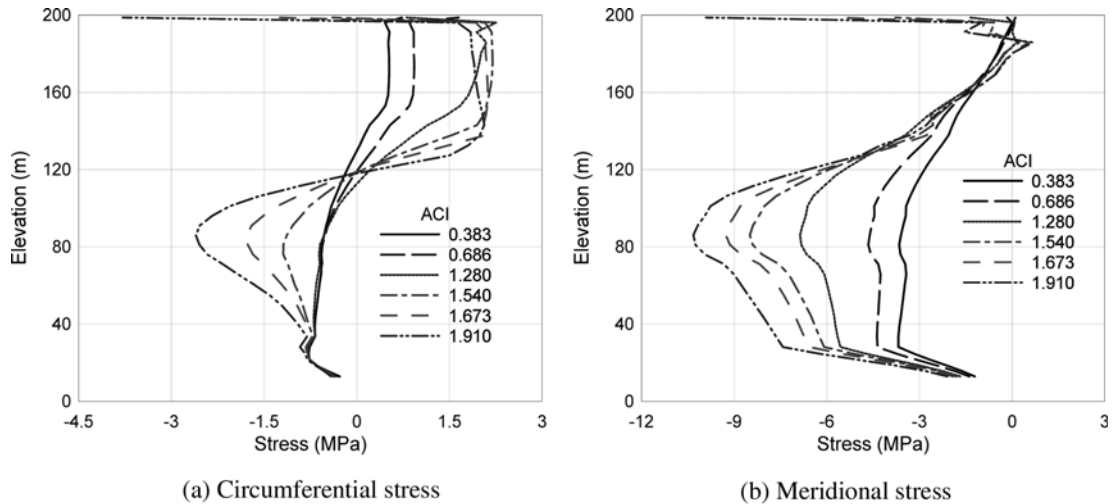


Fig. 15 Stresses in the array of elements along the meridian ($\theta = 30^\circ$ from the stagnation)

the stresses evaluated with the ACI loading is given here. In Figs. 13-15, the stresses at the outermost layer are given.

The stress redistributions as a function of load factor at the throat level are given in Fig. 13. As is seen in Fig. 13, the compressive stress in the circumferential direction at the windward part exceeds the initial yield stress of $0.3f_{ck}$ that corresponds to 6.36 MPa. In case of meridional components, there appear some negative (compressive) stresses at the failure load, as is seen in Fig. 13(b). As can be observed in Fig. 14(b), the compressive stresses at the windward part of the cooling tower shell spread in between elevations 100 m and 140 m (the throat level). To explain this result, we need to take into account the various factors such as reinforcing ratio, shell thickness, growth of

crack width, and the effect of stress redistribution. As already demonstrated in Fig. 12, the crack width at the throat increased abruptly once the crack is occurred at the load factor of 1.53. This is caused by the minimum thickness (210 mm) and small amount of reinforcement at this elevation, and means that the increase in loading after the load factor of 1.53 just pushes the part upper the throat up without pulling the shell below the throat. Naturally, it seems that this behavior is caused by the small thickness, insufficient reinforcement. In case of the cooling tower in the ordinary size, smaller than 150 m in height, this phenomenon does not appear (Milford 1984, Noh 2005).

Figs. 14 and 15 illustrate the stress distribution in the array of elements along the meridian at the circumferential degree of $\theta = 0^\circ$ and $\theta = 30^\circ$, respectively. The stresses that exceed the initial yield stress appear in several places (Fig. 14(a), Fig. 15(b)) and gradual redistribution of stress is observed. From Fig. 14(b), it can be noticed that the gravity load due to self-weight of reinforced concrete counteracts about 50% of the design wind load. That is, the meridional stress that reaches zero level occurs first at the load factor of about 0.5. Therefore, it is clear that the self-weight of the cooling tower plays an important role of ensuring *a priori* safety to cooling tower structures.

In passing, it has to be noticed that since a revised version of VGB-guideline has been published in April 2005, this new guideline has to be taken into consideration if the results given in this paper are to be referred.

6. Conclusions

A nonlinear behavior from the unstressed virgin state to the ultimate state is given for Niederaussem RC cooling tower shell. In order for the analysis scheme to include material nonlinearities in concrete, various nonlinear factors such as work-hardening plasticity, tensile cracking, crack rotation, tension stiffening, and shear transfer are taken into account. The geometrical nonlinearity based on Green-Lagrange strain tensor is also considered. Besides, the damage process of the cooling tower structure is observed introducing the damage index that is defined in terms of a current stiffness index.

Based on the results of numerical analyses, the two guidelines, VGB-guidelines in Germany and ACI-code in the US, are examined as similar to each other in general. The main difference comes from the discrepancy in considering the wind profile: the exponents employed in the equation with which the effect of the elevation on the wind pressure is taken into account are different with each other. It has to be noticed, however, that the exponent depends on the condition of the terrain on which the cooling tower is erected. Consequently, even though the wind pressures of each guideline have different scales, the two guidelines are examined as highly correlated to each other when they are seen from the perspective of their quality.

The ultimate load of the Niederaussem cooling tower is evaluated as 2.254(VGB) and 1.910(ACI) times that of the design wind load, at the damage level of about 80%. The effect of internal suction is observed as negligible, even though it affects the quantity of the wind pressure by shifting the wind pressure that corresponds to 0.5 of wind pressure coefficient. The failure of the cooling tower is investigated as triggered by the yielding of reinforcement in the vicinity of the throat, not in the part where the first crack occurred. This phenomenon is observed in detail by means of investigation on the mean crack width that is defined using the total principal strains.

References

- ACI-ASCE committee 334 (1985), Reinforced Concrete Cooling Tower Shells – Practice and Commentary.
- Busch, D., Harte, R., Krätzig, W.B. and Montag, U. (2002), “New natural draft cooling tower of 200 m of height,” *Eng. Struct.*, **24**(12), 1509-1521.
- Choi, C.K. and Paik, J.G. (1994), “An efficient four node degenerated shell element based on the assumed covariant strain”, *Struct. Eng. Mech.*, **2**(1), 17-34.
- Choi, C.K. and Paik, J.G. (1996a), “An effective four node degenerated shell elements for geometrically nonlinear analysis”, *Thin-Walled Structures*, **24**(3), 261-283.
- Choi, C.K. and Noh, H.C. (1996b), “Analysis of geometrically imperfect cooling tower shell considering the effect of tension stiffening of concrete”, *Proc. of the 4-th Int. Symposium on Natural Cooling Towers*.
- Choi, C.K. and Noh, H.C. (1999), “Simulation of wind process by spectral representation method and application to cooling tower shell”, *Wind and Structures*, **2**(2), 105-117.
- Cotsovos, D.M. and Pavlovic, M.N. (2005), “Numerical investigation of RC structural walls subjected to cyclic loading”, *Computers and Concrete*, **2**(3), 215-238.
- Crisfield, M.A. (1983), “An arc-length method including line searches and accelerations”, *Int. J. for Numer. Meth. Eng.*, **9**, 1269-1289.
- Hand, F.R., Pecknold, D.A. and Schnobrich, W.C. (1973), “Nonlinear layered analysis of RC plates and shells”, *J. Struct. Div.*, ASCE, **99**(ST7), 1491-1505.
- Hara, T., Kato, S. and Nakamura, H. (1994), “Ultimate strength of RC cooling tower shells subjected to wind load”, *Eng. Struct.*, **16**(3), 171-180.
- Harte, R., Krätzig, W.B., Noh, S.Y. and Petryna, Y.S. (2000), “On progressive damage phenomena of structures”, *Comput. Mech.*, **25**, 404-412.
- Hinton, E. and Owen, D.R.J. (1984), *Finite Elements Software for Plates and Shells*, Pineridge Press, Swansea, U.K.
- Kwak, H.G. and Kim, D.Y. (2004), “Cracking behavior of RC shear walls subject to cyclic loadings”, *Computers and Concrete*, **1**(1), 77-98.
- Gupta, A.K. and Akbar, H. (1984), “Cracking in reinforced concrete analysis”, *J. Struct. Eng.*, ASCE, **110**(8), 1735-1746.
- Lin, C.S. and Scordelis, A.C. (1975), “Nonlinear analysis of RC shell of general form”, *J. Struct. Div.*, ASCE, **101**(3), 523-538.
- Mahmoud, B.E.H. and Gupta, A.K. (1993), “Inelastic large displacement behavior and buckling of hyperbolic cooling tower shells”, Research Program on Nuclear Power Plant Structures, Equipment and Piping.
- Milford, R.V. and Schnobrich, W.C. (1984), “Nonlinear behavior of reinforced concrete cooling towers”, Civil Engng. Studies Structural Research Series No. 514, University of Illinois.
- Min, C.S. and Gupta, A.K. (1992), “A study of inelastic behavior of reinforced concrete shells using supercomputers”, Dept. of Civil Engng. North Carolina State University at Raleigh.
- Noh, H.C. (2005), “Ultimate strength of large scale reinforced concrete thin shell structures”, *Thin-Walled Structures*, **43**(9), 1418-1443.
- Noh, H.C. (2006), “Nonlinear behavior and ultimate load bearing capacity of reinforced concrete natural draught cooling tower shell”, *Eng. Struct.*, **28**(3), 399-410.
- Noh, S.Y., Meskouris, K., Harte, R. and Krätzig, W.B. (2003), “New design concept and damage assessment of large-scale cooling towers”, *Struct. Eng. Mech.*, **15**(1), 53-70.
- Owen, D.R.J. and Hinton, E. (1980), *Finite Elements in Plasticity*. Pineridge Press Limited, Swansea, U.K.
- VGB-Guidelines (1997), “Structural design of cooling towers”, VGB-Technical Committee Essen, Germany.
- Zahlten, W. and Borri, C. (1998), “Time-domain simulation of the non-linear response of cooling tower shells subjected to stochastic wind loading”, *Eng. Struct.*, **20**(10), 881-889.